




Airborne GNSS-R Polarimetric Multiincidence Data Analysis for Surface Soil Moisture Estimation Over an Agricultural Site

Mehrez Zribi , Senior Member, IEEE, Vincent Dehaye, Karin Dassas , Pascal Fanise, Michel Le Page , Pierre Laluet, and Aaron Boone

Abstract—The objective of this study is to propose a mapping of surface soil moisture (*SSM*) using airborne measurements based on the Global Navigation Satellite System Reflectometry Instrument, a polarimetric instrument. GNSS-R measurements were acquired at the agricultural Urgell site in Spain in July 2021. In situ measurements describing the soil moisture and roughness and the vegetation cover leaf area index were then obtained simultaneously with flight measurements. An analysis of observable copolarization (right–right) reflectivity Γ_{RR} and the cross-polarization (right–left) reflectivity Γ_{RL} behaviors as a function of incidence angle is proposed, as is normalization of the reflectivity function of the incidence angle. The sensitivity of reflectivities is then proposed as a function of surface soil moisture. An empirical model with two variables, soil moisture, and the normalized difference vegetation index, based on the principle of the tau–omega model is then considered for the inversion of GNSS-R reflectivity Γ_{RL} and estimation of soil moisture. This model is calibrated and validated by a threefold cross-validation approach. A mapping of *SSM* at 100 m resolution is created with data from the studied site and three acquired flights.

Index Terms—Airborne, Global Navigation Satellite System Reflectometry Instrument, GNSS-R, inversion, surface soil moisture.

I. INTRODUCTION

SURFACE soil moisture is a key parameter in understanding the function of the soil–vegetation–atmosphere interface. It is also an essential parameter in the management of water resources related to irrigation [1], [2], [3], [4].

Over the past 30 years, microwave remote sensing has shown great potential for estimating and monitoring this parameter [5], [6], [7].

Manuscript received 7 July 2022; revised 23 August 2022 and 15 September 2022; accepted 16 September 2022. Date of publication 23 September 2022; date of current version 7 October 2022. This work was supported in part by the French National Research Agency through HILIAISE ANR-19-CE01-0017 Project, in part by the French Space Study Center through SCOMAG Project, and in part by the Horizon 2020 ACCWA Project through the Marie Skłodowska-Curie Research and Innovation Staff Exchange (RISE) Program under Grant Agreement 823965. (Corresponding author: Mehrez Zribi.)

Mehrez Zribi, Vincent Dehaye, Karin Dassas, Pascal Fanise, Michel Le Page, and Pierre Laluet are with Centre d'Etudes Spatiales de la Biosphère (CNES/CNRS/INRAE/IRD/UPS), 31401 Toulouse Cedex 9, France (e-mail: mehrez.zribi@ird.fr; vincent.dehaye@univ-tlse3.fr; karine.dassas@univ-tlse3.fr; pascal.fanise@ird.fr; michel.le_page@ird.fr; pierre.laluet@univ-tlse3.fr).

Aaron Boone is with Météo-France/CNRS, CNRM-Université de Toulouse, 31057 Toulouse Cedex 1, France (e-mail: aaron.a.boone@gmail.com).

Digital Object Identifier 10.1109/JSTARS.2022.3208838

Various operational products have been offered in recent years, ranging from the scale of an agricultural plot to the scale of several kilometers.

In this same context, GNSS-R measurements have also shown great potential for characterizing earth surface states [8], [9], [10], [11] and, particularly, surface soil moisture [12], [13], [14], [15], [16], [17], [18], [19], [20], [21]. These measurements started first with in situ or airborne campaigns, illustrating good precision in the estimation of soil moisture and vegetation cover biomass at the same level as other active or passive microwave techniques [14], [15], [22], [23], [24].

These studies mainly analyze data acquired in right–left (RL) polarization. During the Land Monitoring with Navigation Signals (LEIMON) campaign, with acquisitions in Italy, the sensitivity of Γ_{RL} signals to surface soil moisture (*SSM*) was between 20 and 30 dB/(m³/m³). This result was confirmed during the GNSS Reflectometry Analysis for biomaSS monitoring (GRASS) campaign carried out in Italy, with a sensitivity confirmed to be on the order of 20 dB/(m³/m³) and a determination coefficient between the ground moisture measurements and the GNSS-R reflectivity polarization ratio equal to 0.86. Egido et al. [14] also demonstrated the potential of GNSS-R data to estimate *SSM* during airborne measurements with the light airborne reflectometer for GNSS-R observations instrument at a Spanish site. An empirical model relating soil moisture, surface temperature, a vegetation index, and reflectivity is proposed. This study was restricted to soil moisture levels below 0.15 m³/m³. The high sensitivity of reflectivity to *SSM* was also retrieved during campaigns carried out in southwestern France with the GLORI airborne instrument in 2015 [24]. The potential of GNSS-R was later confirmed by satellite receivers with early work with the Technology Demonstration Satellite (Techdemosat) [25], [26], [27], [28], [29], followed by numerous results from the Cyclone Global Navigation Satellite System (CYGNSS) constellation, which was launched in 2016 [30]. Camps et al. [29] analyzed the relationships between TechDemosat data and *SSM*. The sensitivity of GNSS-R signals to soil moisture remains on the same order of magnitude as airborne measurements (~38 dB/(m³/m³)). The sensitivity of TechDemosat data to *SSM* is also observed in [26] with a 7 dB dynamic due to changes in *SSM*. With CYGNSS, the potential of GNSS-R satellite data was quickly highlighted for monitoring flooded areas, monitoring biomass, even at very

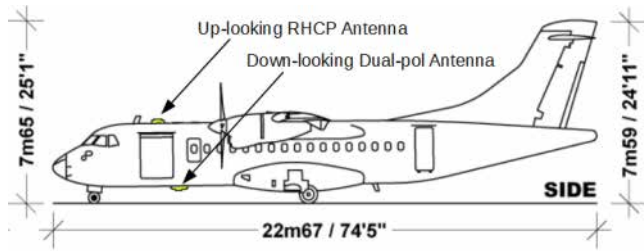


Fig. 1. GLORI antenna locations on ATR-42.

high levels, and finally monitoring soil moisture [31], [32], [33], [34], [35], [36], [37], [38], [39], [40], [41]. Chew and Small [31] identified a strong correlation between temporal variations in *SSM* and *CYGNSS* signals. A bilinear regression model is thus proposed for the estimation of soil moisture. Trilinear regression including vegetation, roughness, and *SSM* is proposed for the inversion of reflectivity at a quasiglobal scale [32]. Regression calibration is developed independently for each pixel. These cited studies are generally developed with the observable Γ_{RL} . Despite the high potential of these GNSS-R data, the interpretation of the measurement behavior is still a subject of research. Indeed, the angular effects, as well as the particularities of the two polarizations (right-left), *RL*, and (right-right) *RR*, for different land surface contexts, are not yet fully understood, particularly for refining the inversions and better decorrelating the effects of soil moisture, vegetation, and possibly other factors. In this context, theoretical simulators are very useful for understanding all these multiconfiguration behaviors [42], [43]. Numerous studies have also proposed confirming the potential of GNSS-R polarimetry, showing very encouraging results for the estimation of surface characteristics such as vegetation, soil moisture, and flooded areas [44], [45], [46], [47], [48].

The objective of this study is to propose new airborne measurements using real data to refine this understanding. This process involves analyzing polarimetric multiincidence GNSS-R airborne data over an agricultural site with the goal of mapping *SSM*.

Section II presents the airborne and in situ data acquired at the study site in Spain and the observables measured by the GLORI instrument. Section III describes inversion modeling to estimate soil moisture. Section IV presents the discussion. Finally, Section V concludes this article.

II. DATABASE AND METHODS

A. GNSS-R Airborne Data

The GLORI instrument described in [23] is derived from the conventional GNSS-R (cGNSS-R) family. It is a low-cost, 4-channel, highly versatile GNSS-R receiver built using mainly commercial off-the-shelf components. Measurements of direct and reflected GNSS signals are realized by two hemispherical GPS L1-L2 dual-polarization active antennas, named the zenith antenna, which is mounted on the upper part of the aircraft fuselage, and the nadir antenna, which is mounted on the lower fuselage of the aircraft (see Fig. 1). The polarimetric instrument

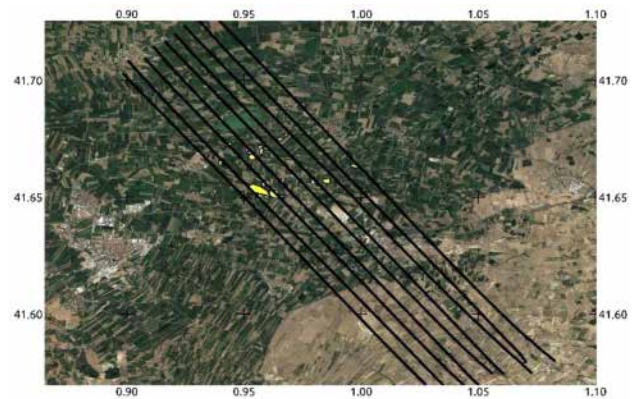


Fig. 2. Location of the GLORI flights in the Urgell Basin, with reference fields in yellow.

allows simultaneous acquisition of left-hand circular polarization (LHCP) and right-hand circular polarization (RHCP) and a complete analysis of the polarization effect on land surface characterization. Measurements are realized with the French research aircraft ATR-42. The received signals are then filtered to reduce out-of-band noise, which can saturate the front end. The radio frequency (RF) signals are fed into a 4-channel L-band front end, which ensures direct IQ downconversion, 2-bit signal decimation, and serialization to a USB 2.0 interface. Raw data signals are acquired with a standard PC. All computations, signal tracking, and retrieval of observables are performed after the flights. The main technical specifications of the instrument are presented in [23].

The GLORI campaigns are realized over the Urgell site in Catalonia, Spain (see Fig. 2). It is an agricultural area composed of two parts, the first of which uses intensive irrigation. The irrigation water comes from the Pyrenees through the Urgell canal. Three different irrigation methods can be identified: 1) flooding, which is still dominant in this region and is used for multiple crops, including fruit trees (apple and pear orchards) and cereals; 2) sprinkler irrigation (pivot, ramp, and integral), which is mainly used for alfalfa and cereal crops (maize, barley, and wheat); and 3) localized irrigation (mainly drip irrigation), which is mainly used for vegetables. A second part of the area is rainfed. The climate is in the Köppen-Geiger zone, a cold, semiarid climate bordering the Mediterranean Sea. It has mild winters, very dry and warm summers and two rainy seasons in autumn and spring. The GLORI campaign was spread over a period of one week (see Table I) and linked with simultaneous, collocated ground-truth measurements.

In parallel with the GLORI GNSS-R airborne acquisitions, various in situ measurements were made on these sites (roughness, soil moisture, and leaf area index) to validate the GLORI data and optimize the inversion algorithms.

B. In situ and Satellite Data

Intensive, collocated ground-truth measurements were recorded at the same time that the flights were made over the 24 reference fields (eight maize, four bare soils, six alfalfa, and four apple trees). The in situ measurements made at the reference

TABLE I
SUMMARY OF THE GLORI CAMPAIGN CHARACTERISTICS

Flight id	Date	Start (UTC)	End (UTC)	Flight Duration
45	22/07/21	10:38:10	14:50:05	04:11:55
46	27/07/21	10:23:54	14:28:32	04:04:38
47	28/07/21	10:23:45	14:27:36	04:03:51

TABLE II
GROUND MEASUREMENTS DURING GLORI CAMPAIGNS

	<i>Hrms</i> (cm)	<i>Lc</i> (cm)	M_v (m ³ /m ³)	<i>LAI</i> (m ² /m ²)
22/07/2021	[0.4–1.84]	[4–12.18]	[0.06–0.34]	[0–3.14]
27/07/2021	–	–	[0.12–0.40]	–
28/07/2021	–	–	[0.1–0.43]	[0.14–3.42]

fields (see Fig. 2) were designed to determine the soil moisture, roughness, and vegetation characteristics. These measurements are realized in the context of the LIAISE international project [49].

1) *Soil Moisture*: On each of the dates listed in Table I, approximately 20 handheld thetaprobe measurements were made in each reference field (irrigated or nonirrigated) at a depth of 5 cm. The samples were taken from various locations in each reference field within a four-hour time frame of the concurrent airborne acquisitions. The thetaprobe measurements were calibrated with gravimetric measurements recorded during previous campaigns [50], [51]. In the context of a homogeneous agricultural field, these in situ measurements should allow a mean accuracy better than 0.02 m³/m³.

2) *Soil Roughness*: The soil roughness was characterized with a 1-m pin profiler exhibiting a pin spacing of 2 cm using six roughness profiles (three perpendicular and three parallel profiles with respect to the interrow tillage direction). These profiles were digitized to calculate statistical parameters of the soil roughness, namely, the root mean square of the height (*Hrms*) and correlation length (*Lc*) [52]. *Hrms* varied between 0.4 and 1.84 cm, and the *Lc* value varied between 4 and 12.18 cm.

3) *Leaf Area Index (LAI)*: Vegetation cover measurements were performed to characterize the *LAI*. The *LAI* is defined as the total one-sided area of leaf tissue per unit ground surface area. According to this definition, the *LAI* is a dimensionless quantity. For each test field, ten hemispherical digital images were used. These were processed by analyzing the canopy gap fraction to retrieve this vegetation parameter. The measurements were applied two times during the intense experimental period. During all measurement campaigns, the computed *LAI* value ranged between 0 and 3.42. The highest values of *LAI* were observed mainly in irrigated test fields. Table II shows the ranges of all acquired in situ measurements over reference fields.

4) *Sentinel-2 Data*: After the launch of Sentinel-2 (S-2) A and B on 23/06/2015 and 07/03/2017, respectively, optical data

became free and open access with a spatial resolution varying between 10 m × 10 m and 60 m × 60 m and a revisit time of up to 5 days in 13 spectral bands at visible and mid-infrared wavelengths. In this study, we used S-2 surface reflectance products downloaded from the Theia site (<https://www.theia-land.fr/>), already orthorectified and atmospherically corrected with a mask of clouds and shadows owing to the MAJA algorithm.

On each acquisition date and using red visible and near-infrared bands with center wavelengths of approximately 665 and 833 nm, respectively, we calculated the *NDVI* and averaged this index for each reference field as expressed in the following:

$$NDVI = \frac{R_{NIR} - R_{Red}}{R_{NIR} + R_{Red}} \quad (1)$$

where R_{NIR} and R_{Red} are the surface reflectance in the two bands, near infrared and red visible, respectively.

C. GNSS-R Data Processing

1) *Observables*: Different observables were obtained from the GLORI measurements. The direct and reflected GNSS signals, $u_{d,r}$ and $u_{r,r}$, respectively, were cross correlated with pseudorandom noise (PRN) code replicas $a(t)$, resulting in direct and reflected complex delay Doppler maps $Y(\tau, f)$, which are considered to be the fundamental observables in the GNSS-R measurements. The cross-correlated signals can be written in the following form:

$$Y(\tau, f) = \frac{1}{T_i} \int_{T_i} u_{d,r} a(t - \tau) e^{i(f_c + f)t} dt \quad (2)$$

where T_i ($= 5$ ms in the present case) is the coherent integration time. For the direct signal, τ corresponds to the signal propagation delay from the transmitter to the receiver, f_c is the GPS L1 frequency, and f corresponds to the Doppler shift resulting from the velocity of the aircraft relative to that of the GNSS satellite.

The geophysical analysis cannot be realized directly from complex waveforms. Incoherent integration is then added to reduce the speckle noise from reflected signals. This step is illustrated by

$$\begin{aligned} \langle |Y(\tau, f)|^2 \rangle &= \frac{T_i^2 Pt Gt \lambda^2}{(4\pi)^3} \iint_A \frac{Gr(\vec{\rho})}{R_0^2(\vec{\rho}) R^2(\vec{\rho})} \\ &\times \sigma_{pq}^0 \chi^2(\vec{\rho}, \delta\tau, \delta f) d\vec{\rho} \end{aligned} \quad (3)$$

where Pt and Gt are the satellite transmit power and antenna gain, respectively, λ is the signal wavelength, $Gr(\vec{\rho})$ is the receiving antenna gain, $R_0(\vec{\rho})$ and $R(\vec{\rho})$ are the distances from the specular point to the transmitter and the receiver, respectively, σ_{pq}^0 is the polarization-dependent bistatic radar coefficient, and χ is known in the radar terminology as the Woodward ambiguity function (WAF) and accounts for the radar pulse characteristics.

$Y(\tau, f)$ is referred to as a delay Doppler map (DDM), corresponding to the average value of the GNSS power scattered by the surface as a function of delay and frequency.

Finally, we consider the apparent reflectivity based on the calculation of the relative power of the reflected signal compared to the direct signal.

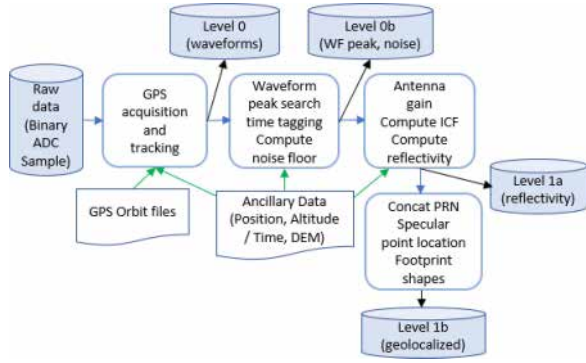


Fig. 3. Processing block diagram.

For a polarization pq , the apparent reflectivity Γ_{pq} can be expressed as the ratio of the reflected $Y_{r,q}(\tau, f)$ to direct waveforms $Y_{d,p}(\tau, f)$.

In the case of GNSS-R, the right–right and right–left ratios Γ_{RR} and Γ_{RL} represent the co and cross-polar reflection coefficients. Assuming that f is aligned with the Doppler frequency shift of the direct signal, the apparent surface reflectivity Γ'_{pq} can be obtained as

$$\Gamma'_{pq} = \left| \left\langle \frac{Y_{r,q}(\Delta\tau, f)}{Y_{d,p}(0, f)} \right\rangle \right|^2 \quad (4)$$

where $\Delta\tau$ represents the difference in delay between the direct and reflected paths.

In GLORI data processing, the apparent reflectivity Γ'_{pq} is calculated in a way that allows for the separation of coherent and incoherent components using the interferometric complex field (ICF), corrected using the differences in noise and antenna gain between the direct and reflected channels [23].

2) *Processing Steps*: Four steps are considered to process the raw data (see Fig. 3) and to generate different data products:

- 1) The first step is to calculate coherently integrated direct and reflected waveforms. The considered integration time is 5 ms. The direct GPS signal is acquired and tracked from the measurements of the zenith-pointing antenna, while the reflected signals measured by the nadir-pointing antenna are processed according to a master–slave scheme using the tracking parameters from the direct signal. From these measurements, in addition to metadata and information relating to decoded GPS messages, level 0 (L0) files are generated.
- 2) From the L0 level to the L0b level, the waveforms are precisely time-tagged from the GPS message, the waveform maxima are detected, and the waveform noise floor is computed.
- 3) From L0b to L1a, the corrected ICFs are computed for each polarization and coherent integration time step. Then, the ICFs are incoherently averaged (200 ms), and their standard deviation is estimated to be able to compute the apparent reflectivity. All useful information, such as attitudes and the relative position of the emitter, interpolated in the integration step in addition to calibration factors,

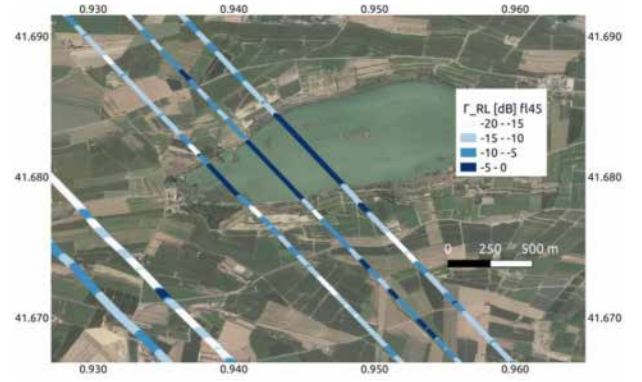


Fig. 4. Γ_{RL} measurements over the Urgell site. The aircraft altitude is ~ 1100 m, and the measurement temporal resolution (incoherent averaging time) is 200 ms.

such as the antenna radiation pattern, are stored in level 1a files (L1a).

- 4) L1a files are then aggregated into Level 1b (L1b) files for each flight. They include all of the calibration information in addition to other ancillary parameters. From the auxiliary data, the location and shape of the specular ellipses corresponding to the first Fresnel zone are also calculated.

Fig. 4 illustrates the processed signals for the different transects. As presented in the processing steps, illustrated areas correspond to specular points with calculated first Fresnel zones [9]. For each reference field, the measurements acquired by the GLORI instrument are averaged to obtain an estimate of the reflectivities. From the observed values, we note qualitative trends, particularly for the highest signatures on a small lake located west of the study site. This is obviously specular background with maximum reflectivity.

III. RESULTS

A. Normalization of the Reflectivity Function of Incidence

Fig. 5 illustrates the variations in all the acquired GLORI reflectivity data over the Urgell site as a function of the incidence angle. As demonstrated in [23], the cross-polarization isolation is better than 15 dB at angles up to 45° from bore-sight (45° incidence angle) for both LHCP and RHCP ports. A cross-polarization performance of less than 15 dB is considered inadequate for polarimetric measurements [21]. In this study, analysis is proposed up to a 60° incidence angle because we do not observe any particular anomaly in data higher than 45° (cross-polarization isolation is still higher than 10 dB for considered angles). We observe weak variations for the case of Γ_{RL} and a stronger variation for the case of gamma Γ_{RR} . To better understand the effect of incidence angle on reflectivity, we propose this analysis according to the NDVI, with a window of 0.2 to allow the evaluation of trends. Concerning Γ_{RL} , we propose linear approximation of the observed variation function of the incidence angle

$$\Gamma_{RL} = a(NDVI) + b(NDVI) \cdot \theta \quad (5)$$

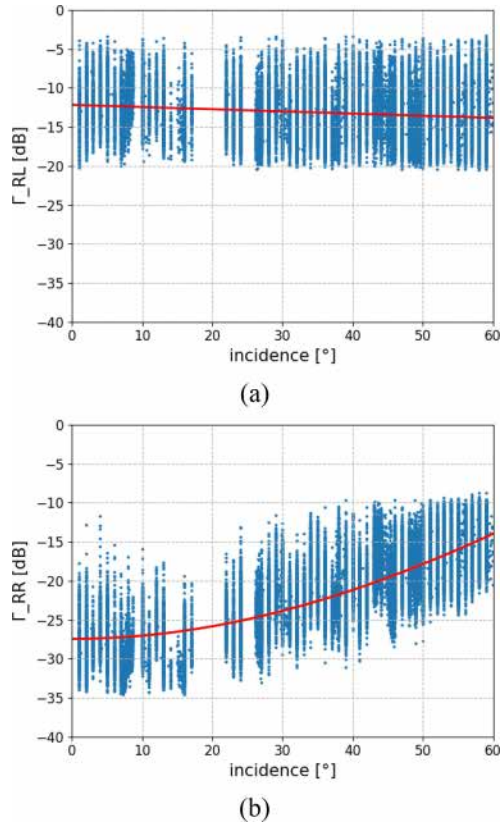


Fig. 5. Illustration of GLORI reflectivity data over the Urgell site as a function of incidence angle: (a) Γ_{RL} and (b) Γ_{RR} .

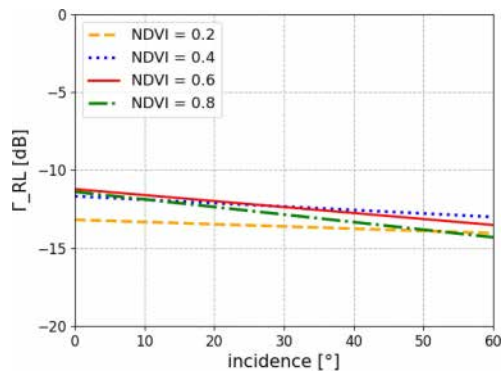


Fig. 6. Illustration of empirical fitting relationships between Γ_{RL} and incidence angles for different $NDVI$ classes.

where parameters a and b are functions of $NDVI$.

We consider the hypothesis of an identical SSM range for all $NDVIs$ and incidence angles to avoid considering the effect linked to moisture levels.

Fig. 6 illustrates the linear approximations for each $NDVI$ interval. We clearly observe a decrease in the b parameter and slope of the linear relationship with the $NDVI$. Indeed, on bare soils, an almost zero slope is observed, which decreases slightly with the $NDVI$. The slope parameter decreases from -0.014 to -0.048 dB/°. Initially, for bare soils, there is a slight effect linked to the Fresnel coefficient due to the generally low roughness, as illustrated in ground measurements. This effect increases with

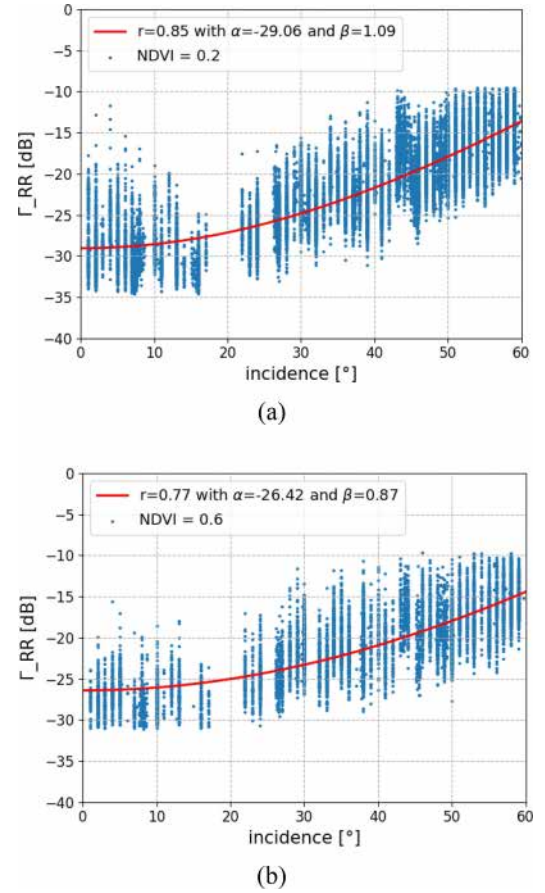


Fig. 7. Illustration of the Γ_{RR} variation function of the incidence angle for two $NDVI$ classes: (a) $NDVI = 0.2$ and (b) $NDVI = 0.6$.

the development of the vegetation cover and the introduction of an attenuation effect that changes with the incidence angle.

Regarding the behavior of the Γ_{RR} measurements as a function of the incidence angle, we propose an empirical relationship of the following form:

$$\Gamma_{RR} = \alpha(NDVI) \cdot (\cos\theta)^{\beta(NDVI)} \quad (6)$$

where α and β parameters are functions of $NDVI$.

Fig. 7 illustrates the approximations of these relationships for different $NDVI$ classes. A decrease in the angular effect is observed with increasing $NDVI$. The difference in reflectivity levels between 0 and 50° for almost bare soil ($NDVI = 0.2$) is approximately 11 dB and reaches a value close to 8 dB for an $NDVI$ equal to 0.8 . The largest differences between signatures of the different $NDVI$ classes are observed at low incidence angles. These differences decrease to almost zero for angles close to 50° , as illustrated in Fig. 8. These strong angular trends for Γ_{RR} show the importance of considering the incidence angle in the analysis of these data. This also highlights a much greater potential to monitor the dynamics of the vegetation cover for low incidence angles.

Based on these results, we propose normalization of the data to a single incidence angle of 20°

$$\Gamma_{RL}(20^\circ) = \Gamma_{RL}(\theta) + b(NDVI)(\theta - 20^\circ) \quad (7)$$

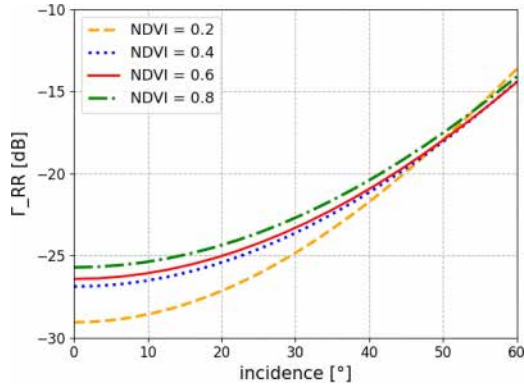


Fig. 8. Illustration of empirical fitting relationships between Γ_{RR} and incidence angles for different $NDVI$ classes.

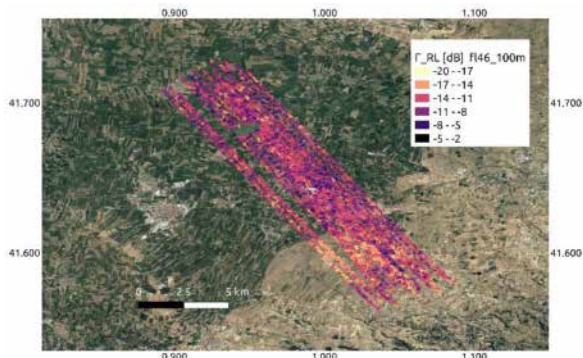


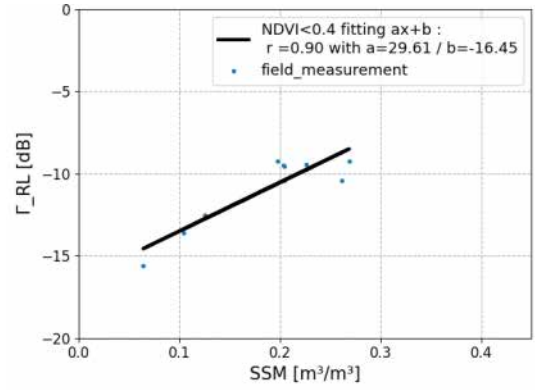
Fig. 9. Map of Γ_{RL} over the studied site.

$$\Gamma_{RR}(20^\circ) = \Gamma_{RR}(\theta) \left(\frac{\cos(20^\circ)}{\cos(\theta)} \right)^{\beta(NDVI)} \quad (8)$$

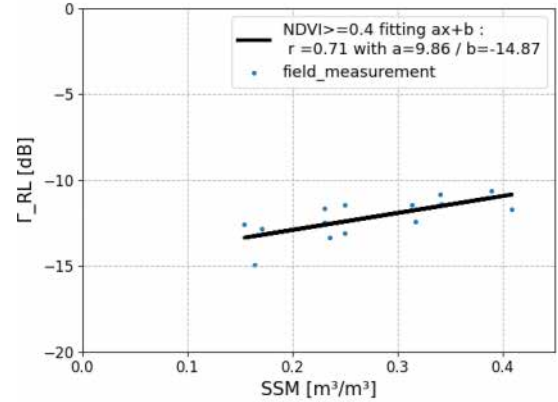
This normalization aims to clearly limit the angular effects, particularly for Γ_{RR} , and thus to characterize the effects due to land surface properties with higher precision. Hence, for each $NDVI$ class, we apply the retrieved linear relationship for Γ_{RL} and the cosine relationship for Γ_{RR} . From normalized data, we finally propose a 100 m mesh to build maps of observables. For each mesh, we average all the measurements acquired with different PRNs. Fig. 9 illustrates the map of Γ_{RL} .

B. Sensitivity of Reflectivity to Surface Soil Moisture

Figs. 10 and 11 illustrate Γ_{RL} and Γ_{RR} reflectivities over reference fields as a function of SSM ground measurements. An analysis of two vegetation classes, $NDVI < 0.4$ and $NDVI > 0.4$, is proposed to limit the effects related to vegetation cover. We first observe a sensitivity that decreases with the development of the vegetation cover. In the case of Γ_{RL} , this sensitivity decreases from 29.61 dB/(m³/m³) for the class with $NDVI < 0.4$ to 9.86 dB/(m³/m³) for the densest class. These sensitivities are consistent with the results found in other airborne campaigns, such as GLORI'2015, LEIMON, and GRASS. For the case of RR polarization, in the case of the two classes of vegetation, we observe extremely low sensitivities of reflectivity to soil moisture, with correlations that are very degraded (less than 3.12 dB/(m³/m³)). These results could be explained by the



(a)



(b)

Fig. 10. Analysis of Γ_{RL} sensitivity to soil moisture for two vegetation classes: (a) $NDVI < 0.4$ and (b) $NDVI > 0.4$.

weakness of the RR signal over agricultural surfaces and by a higher vegetation effect with RR than with RL polarization. In conclusion, these results clearly illustrate a much greater potential for soil moisture monitoring using Γ_{RL} reflectivity data. In the following, the estimation of the moisture is limited to this last polarization.

C. Reflectivity Semiempirical Modeling

The reflectivity can be modeled by

$$\Gamma_{pq}(\theta) = \Gamma_{pq}^{soil}(\theta) \cdot e^{-\frac{2\tau_p^{canopy}}{\sin\theta}} (1 - \omega_p^{canopy})^2 \quad (9)$$

where Γ_{pq} is the reflection coefficient for circularly polarized (pq) radiation, $2\tau_p^{canopy}$ is the two-way vegetation opacity, $(1 - \omega_p^{canopy})^2$ accounts for the two-way path of the GNSS signal, θ is the incidence angle, and ω_p^{canopy} is the single scattering albedo.

Various works have used the $NDVI$ optical index as a proxy to describe the dynamics of vegetation cover and thus to estimate the optical thickness. In this study, the LAI *in situ* measurements only served qualitatively to situate the development of the covers. In the modeling of reflectivity, the $NDVI$ seems the most suitable for the highest applicability of methodologies

$$\tau_{pq} = c \cdot NDVI \quad (10)$$

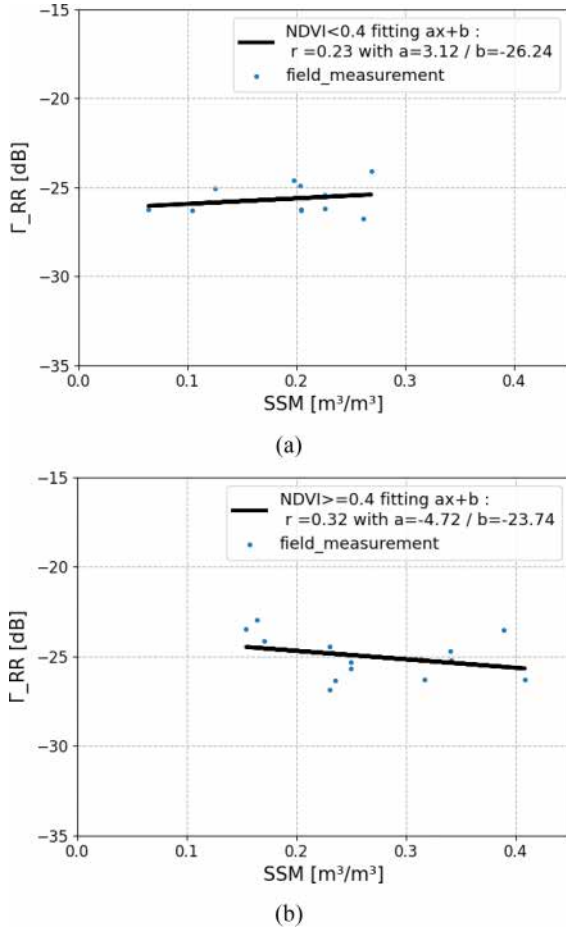


Fig. 11. Analysis of Γ_{RR} sensitivity to soil moisture for two vegetation classes: (a) $NDVI < 0.4$ and (b) $NDVI > 0.4$.

where c is a constant applied to all vegetation covers.

The single-scattering albedo is neglected in the context of L-band measurements. Analyzed data are normalized as a function of incidence angle.

Equation (9) can then be simplified to

$$\Gamma_{pq} = \Gamma_{pq}^{soil} \cdot e^{-2c \cdot NDVI} \quad (11)$$

The relationship between reflectivity (in dB) and soil moisture Mv is identified as linear in many works; hence, we consider the following approximation:

$$\Gamma_{RL\,dB}^{soil} = \gamma Mv + \delta \quad (12)$$

Therefore, by applying a logarithmic function to (11)

$$\Gamma_{RL\,dB} = \gamma Mv + \mu NDVI + \delta \quad (13)$$

where γ is the sensitivity of the reflectivity to soil moisture, μ is the sensitivity of the reflectivity to vegetation growth through the $NDVI$, and δ is a constant related to the roughness mean effect. α , β , and δ are empirical parameters retrieved from the experimental data. The parameters γ , μ , and δ are estimated by minimizing the sum of the squared differences between the simulated and measured Γ_{RL} data. In the context of mostly very smooth surfaces due to gravitation irrigation, it is not possible

TABLE III
PARAMETERS OF THE CALIBRATED INVERSION MODEL

	γ	μ	δ	RMSE (dB)
Γ_{RL}	14.9	-5.3	-12.7	1.3

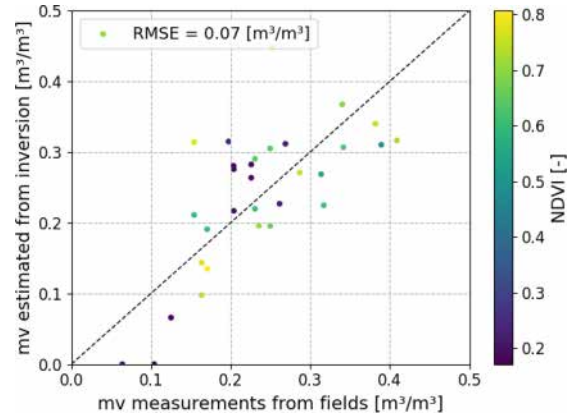


Fig. 12. Intercomparison between ground measurements and estimated soil moisture from Γ_{RL} data inversion.

to establish an empirical relationship between the parameter δ and variations in roughness parameters.

D. Application of the Proposed Semiempirical Model for Soil Moisture Mapping

The inversion model is applied to Γ_{RL} GLORI data. To calibrate and validate the proposed model, we use the threefold cross-validation approach. Our database consists of 31 samples with airborne and ground measurements for reference fields. It is divided into three parts. In these sequential folds, the first was used for validation, and the two remaining folds were used for model parameterization. As in the case of the “repeated holdout” method, the overall accuracy is given by the average of the values obtained from all runs. The model is calibrated and validated three times. The calibration and validation steps are then applied to the whole database.

The calibrated parameters with statistics of comparison between the simulated model and the dataset used for the calibration are shown in Table III.

Thus, if we have Γ_{RL} reflectivity and the $NDVI$ level, the soil moisture is estimated using the following equation:

$$Mv = 0.067 \Gamma_{RL\,dB} + 0.35 NDVI + 0.85 \quad (14)$$

Fig. 12 illustrates the comparison between in situ measurements and estimates from Γ_{RL} data inversion. The retrieved $RMSE$ is equal to $0.07 \text{ m}^3/\text{m}^3$. This reasonable precision illustrates the Γ_{RL} potential to retrieve soil moisture at a high-resolution scale.

A mapping of SSM is proposed from Γ_{RL} map at 100 m resolution. The inversion model is thus used for each mesh considering the Γ_{RL} information and the $NDVI$ calculated from the S-2 data. Three maps are proposed for the three proposed flights acquired

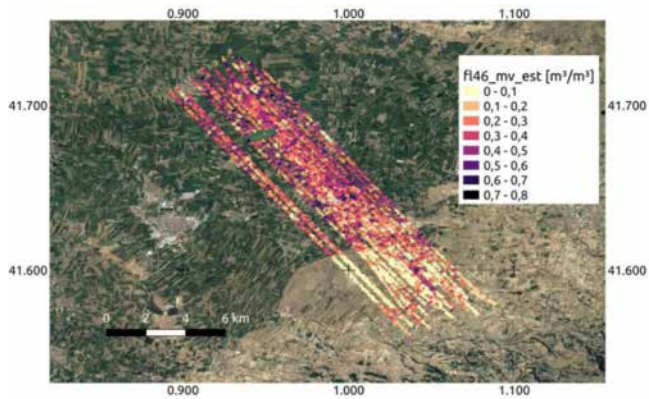


Fig. 13. Map of SSM retrieved from the Γ_{RL} inversion on 27/07/2021, with a spatial resolution equal to 100 m.

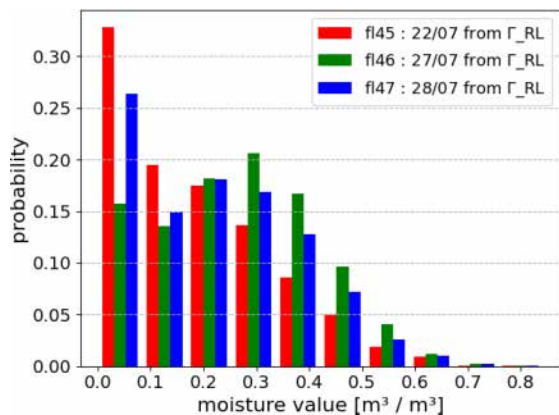


Fig. 14. Illustration of soil moisture level distributions over the Urgell site for three analyzed flights.

on three dates, 22/07/2021, 27/07/2021, and 28/07/2021. The map corresponding to the second date is illustrated in Fig. 13. In all three cases, we first observe a clear contrast between the irrigated and rainfed zones, with higher moisture levels for the first one. This is obviously consistent with our field measurements and water resource use. In the nonirrigated part, we observe a certain homogeneity of the estimates due to the limitation of only rainfall effects and fewer variations in vegetation density.

IV. DISCUSSION

SSM maps are created from the three flights taken on three different dates. The second flight took place just after a rainfall event of 14 mm. This is observed in the temporal variation in SSM levels. Fig. 14 illustrates SSM distributions on the study site for the three dates. We observe a first dry date, 22/07/2021, with a very low moisture level percent. This was illustrated by approximately 32% moisture values below $0.1 \text{ m}^3/\text{m}^3$. 27/07/2021 illustrates a general increase in moisture following 14 mm of precipitation. Thus, the distribution of moisture values significantly changed, with a maximum moisture distribution of approximately $0.3 \text{ m}^3/\text{m}^3$. On the last date, in the context of high heat and temperatures close to 35° during the day, the drop in SSM was quite general, with a return of a higher percentage

of low moisture levels below $0.1 \text{ m}^3/\text{m}^3$ (more than 25%). 28/07 is thus intermediate to the two extremes, a very dry first date and a relatively wet second date.

The proposed inversion approach makes it possible to map soil moisture. However, the sizes of the agricultural fields, which were generally less than 1 ha in the studied site, gravity irrigation of the plots with flooding and, finally, different types of land use affect the precision of the proposed inversion approach. Indeed, mapping at 100 m spatial resolution can include local heterogeneities that are difficult to consider. Despite this relatively complex context, the retrieved precision of approximately $0.07 \text{ m}^3/\text{m}^3$ remains reasonable to respond to thematic studies related to water resource management. The Γ_{RR} reflectivity is not considered for moisture mapping because of its low sensitivity to SSM . However, the limitation of the database and the drop in the data quality for high incidence angles with decreasing cross-polarization isolation excluded a finer analysis of different configurations and confronted the observations with theoretical modeling.

V. CONCLUSION

The objective of this study is to deepen the understanding of the behavior of GNSS-R measurements to propose a high-spatial resolution mapping of surface soil moisture. An airborne campaign using the GLORI instrument is proposed for the Agricultural Urgell site, which consists of two separated irrigated and nonirrigated areas. An analysis of the behavior of GNSS-R reflectivities for the two polarizations RL and RR and as a function of incidence angle is also proposed. The angular effect is demonstrated to be very weak for the case of Γ_{RL} . Linear modeling of this effect seems sufficient, with an effect linked to the development of vegetation cover. Thus, the slope of this relationship is between -0.014 dB° and -0.048 dB° for data ranging from an $NDVI$ close to 0.2 to an $NDVI$ close to 0.8. Regarding reflectivity in RR polarization, the angular effect is much greater, particularly for low incidence angles. A cosine function with two calibrated empirical parameters seems suitable to describe this relationship. For the polarization RL, the angular effect increases with the development of vegetation cover. Normalization of the reflectivity is thus proposed as a function of the incidence angle. As demonstrated by other studies [14], [15], [29], reflectivity illustrates high sensitivity to SSM . For RL polarization, the sensitivity decreases from $29.61 \text{ dB}/(\text{m}^3/\text{m}^3)$ for the class with $NDVI < 0.4$ to $9.86 \text{ dB}/(\text{m}^3/\text{m}^3)$ for the densest class ($NDVI > 0.4$).

A simplified tau-omega model is then proposed to describe the relationship between the measured signals and the two variables SSM and the $NDVI$ of the vegetation. After calibration of the three parameters describing the model with a three-fold cross-validation approach, the validation allowed good precision for Γ_{RL} , with an $RMSE$ of $0.07 \text{ m}^3/\text{m}^3$. Moisture maps were thus created at a spatial resolution of 100 m for each airborne acquisition, illustrating strong differences between irrigated and nonirrigated areas, as well as temporal variations related to precipitation events. In the context of the future launch of the European Space Agency's HYDROGNSS mission, these

measurements should be enriched by other acquisitions covering new configurations, particularly with the L5/E5 configurations, to analyze their contribution to the monitoring of land surface states. Consolidation of cross-polarization isolation for high incidence angles is certainly useful for global analysis of RR polarization potential.

ACKNOWLEDGMENT

The authors would like to thank the technical teams from the SAFIRE, CESBIO, and SAFIRE pilots for their support and contributions to the success of the airborne and ground campaigns.

REFERENCES

- [1] R. D. Koster et al., "Regions of strong coupling between soil moisture and precipitation," *Science*, vol. 305, pp. 1138–1140, 2004.
- [2] S. Manfreda, T. M. Scanlon, and K. K. Caylor, "On the importance of accurate depiction of infiltration processes on modelled soil moisture and vegetation water stress," *Ecohydrogeomorphology*, vol. 3, pp. 155–165, 2009.
- [3] S. Saux-Picart et al., "Water and energy budgets simulation over the Niger super site spatially constrained with remote sensing data," *J. Hydrol.*, vol. 375, pp. 287–295, 2009.
- [4] H. Bazzi et al., "Mapping irrigated areas using sentinel-1 time series in Catalonia, Spain," *Remote Sens.*, vol. 11, no. 15, 2019, Art. no. 1836, doi: [10.3390/rs11151836](https://doi.org/10.3390/rs11151836).
- [5] W. Wagner, G. Lemoine, and H. Rott, "A method for estimating soil moisture from ERS scatterometer and soil data," *Remote Sens. Environ.*, vol. 70, pp. 191–207, 1999.
- [6] R. Fernandez-Moran et al., "SMOS-IC: An alternative SMOS soil moisture and vegetation optical depth product," *Remote Sens.*, vol. 9, 2017, Art. no. 457, doi: [10.3390/rs9050457](https://doi.org/10.3390/rs9050457).
- [7] N. J. Rodríguez-Fernández et al., "Soil moisture retrieval using neural networks: Application to SMOS," *IEEE Trans. Geosci. Remote Sens.*, vol. 53, no. 11, pp. 5991–6007, Nov. 2015.
- [8] M. Martin-Neira, "A passive reflectometry and interferometry system (PARIS)—Application to ocean altimetry," *ESA J.*, vol. 17, pp. 331–355, 1993.
- [9] V. U. Zavorotny, S. Gleason, E. Cardellach, and A. Camps, "Tutorial on remote sensing using GNSS bistatic radar of opportunity," *IEEE Geosci. Remote Sens. Mag.*, vol. 2, no. 4, pp. 8–45, Dec. 2014, doi: [10.1109/MGRS.2014.2374220](https://doi.org/10.1109/MGRS.2014.2374220).
- [10] E. Cardellach, Y. Nan, W. Li, R. Padullés, S. Ribo, and A. Rius, "Variational retrievals of high winds using uncalibrated CYGNSS observables," *Remote Sens.*, vol. 12, 2020, Art. no. 3930.
- [11] N. Pierdicca et al., "Potential of spaceborne GNSS reflectometry for soil moisture, biomass and freeze-thaw monitoring: Summary of an ESA-Funded study," *IEEE Geosci. Remote Sens. Mag.*, vol. 10, no. 2, pp. 8–38, Jun. 2022.
- [12] D. Masters, P. Axelrad, and S. Katzberg, "Initial results of land-reflected GPS bistatic radar measurements in SMEX02," *Remote Sens. Environ.*, vol. 92, pp. 507–520, 2004, doi: [10.1016/j.rse.2004.05.016](https://doi.org/10.1016/j.rse.2004.05.016).
- [13] N. Rodríguez-Alvarez et al., "Soil moisture retrievals using GNSS-R techniques: Experimental results over a bare soil field," *IEEE Trans. Geosci. Remote Sens.*, vol. 47, no. 11, pp. 3616–3624, Nov. 2009.
- [14] A. Egido et al., "Global navigation satellite systems reflectometry as a remote sensing tool for agriculture," *Remote Sens.*, vol. 4, pp. 2356–2372, 2012, doi: [10.3390/rs4082356](https://doi.org/10.3390/rs4082356).
- [15] N. Sánchez et al., "On the synergy of airborne GNSS-R and landsat 8 for soil moisture estimation," *Remote Sens.*, vol. 7, pp. 9954–9974, 2015.
- [16] Y. Pei, R. Notarpietro, P. Savi, M. Cucca, and F. Dovis, "A fully software GNSS-R receiver for soil monitoring," *Int. J. Remote Sens.*, vol. 35, no. 6, pp. 2378–2391, 2014.
- [17] A. Camps et al., "Sensitivity of GNSS-R spaceborne observations to soil moisture and vegetation," *IEEE J. Sel. Topics Appl. Earth Observ. Remote Sens.*, vol. 9, no. 10, pp. 4730–4742, Oct. 2016, doi: [10.1109/JSTARS.2016.2588467](https://doi.org/10.1109/JSTARS.2016.2588467).
- [18] Y. Jia, P. Savi, D. Canone, and R. Notarpietro, "Estimation of surface characteristics using GNSS LH reflected signals: Land versus water," *IEEE J. Sel. Topics Appl. Earth Observ. Remote Sens.*, vol. 9, no. 10, pp. 4752–4758, Oct. 2016.
- [19] S. J. Katzberg, O. Torres, M. S. Grant, and D. Masters, "Utilizing calibrated GPS reflected signals to estimate soil reflectivity and dielectric constant: Results from SMEX02," *Remote Sens. Environ.*, vol. 100, pp. 17–28, 2006, doi: [10.1016/j.rse.2005.09.015](https://doi.org/10.1016/j.rse.2005.09.015).
- [20] Y. Jia and P. Savi, "Sensing soil moisture and vegetation using GNSS-R polarimetric measurement," *Adv. Space Res.*, vol. 59, pp. 858–869, 2017.
- [21] A. Egido, "GNSS reflectometry for land remote sensing applications," Ph.D. Thesis, Universitat Politècnica de Catalunya, Barcelona, Spain, 2013.
- [22] A. Egido et al., "Airborne GNSS-R polarimetric measurements for soil moisture and above-ground biomass estimation," *IEEE J. Sel. Topics Appl. Earth Observ. Remote Sens.*, vol. 7, no. 5, pp. 1522–1532, May 2014, doi: [10.1109/JSTARS.2014.2322854](https://doi.org/10.1109/JSTARS.2014.2322854).
- [23] E. Motte et al., "GLORI: A GNSS-R dual polarization airborne instrument for land surface monitoring," *Sensors*, vol. 16, 2017, Art. no. 732, doi: [10.3390/s16050732](https://doi.org/10.3390/s16050732).
- [24] M. Zribi et al., "Potential applications of GNSS-R observations over agricultural areas: Results from the GLORI airborne campaign," *Remote Sens.*, vol. 10, 2018, Art. no. 1245.
- [25] M. Unwin et al., "GNSS remote sensing and technology demonstration on TechDemoSat-1," in *Proc. 24th Int. Tech. Meeting Satell. Division Inst. Navig.*, Portland, OR, USA, Sep. 2011, pp. 2970–2975.
- [26] C. Chew, R. Shah, C. Zuffada, G. Hajji, D. Masters, and A. J. Mannucci, "Demonstrating soil moisture remote sensing with observations from the U.K. Techdemosat-1 satellite mission," *Geophysical Res. Lett.*, vol. 43, pp. 3317–3324, 2016, doi: [10.1002/2016GL068189](https://doi.org/10.1002/2016GL068189).
- [27] A. Camps et al., "Sensitivity of GNSS-R spaceborne observations to soil moisture and vegetation," *IEEE J. Sel. Topics Appl. Earth Observ. Remote Sens.*, vol. 9, no. 10, pp. 4730–4742, Oct. 2016, doi: [10.1109/JSTARS.2016.2588467](https://doi.org/10.1109/JSTARS.2016.2588467).
- [28] H. Carreno-Luengo, C. Lowe, S. Zuffada, S. Esterhuizen, and S. Oveisgharan, "Spaceborne GNSS-R from the SMAP mission: First assessment of polarimetric scatterometry over land and cryosphere," *Remote Sens.*, vol. 9, 2017, Art. no. 326, doi: [10.3390/rs9040362](https://doi.org/10.3390/rs9040362).
- [29] A. Camps, M. Vall-llossera, H. Park, G. Portal, and L. Rossato, "Sensitivity of TDS-1 GNSS-R reflectivity to soil moisture: Global and regional differences and impact of different spatial scales," *Remote Sens.*, vol. 10, 2018, Art. no. 1856, doi: [10.3390/rs10111856](https://doi.org/10.3390/rs10111856).
- [30] C. Ruf et al., "New ocean winds satellite mission to probe hurricanes and tropical convection," *Bull. Amer. Meteorol. Soc.*, vol. 97, pp. 385–395, 2018, doi: [10.1175/BAMS-D-14-00218.1](https://doi.org/10.1175/BAMS-D-14-00218.1).
- [31] C. C. Chew and E. E. Small, "Soil moisture sensing using spaceborne GNSS reflections: Comparison of CYGNSS reflectivity to SMAP soil moisture," *Geophysical Res. Lett.*, vol. 45, pp. 4049–4057, 2018.
- [32] M. P. Clarizia, N. Pierdicca, F. Costantini, and N. Floury, "Analysis of CYGNSS data for soil moisture retrieval," *IEEE J. Sel. Topics Appl. Earth Observ. Remote Sens.*, vol. 12, no. 7, pp. 2227–2235, Jul. 2019.
- [33] M. Al-Khaldi, J. T. Johnson, A. J. O'Brien, A. Balenzano, and F. Mattia, "Time-Series retrieval of soil moisture using CYGNSS," *IEEE Trans. Geosci. Remote Sens.*, vol. 57, no. 7, pp. 4322–4331, Jul. 2019.
- [34] H. Carreno-Luengo, G. Luzi, and M. Crosetto, "Sensitivity of CYGNSS bistatic reflectivity and SMAP microwave radiometry brightness temperature to geophysical parameters over land surfaces," *IEEE J. Sel. Topics Appl. Earth Observ. Remote Sens.*, vol. 12, no. 1, pp. 107–122, Jan. 2019.
- [35] W. Wan et al., "Using CYGNSS data to monitor China's flood inundation during typhoon and extreme precipitation events in 2017," *Remote Sens.*, vol. 11, 2019, Art. no. 854, doi: [10.3390/rs11070854](https://doi.org/10.3390/rs11070854).
- [36] C. Chew and E. Small, "Description of the UCAR/CU soil moisture product," *Remote Sens.*, vol. 12, 2020, Art. no. 1558.
- [37] Z. Dong and S. Jin, "Evaluation of the land GNSS-Reflected DDM coherence on soil moisture estimation from CYGNSS data," *Remote Sens.*, vol. 13, 2021, Art. no. 570, doi: [10.3390/rs13040570](https://doi.org/10.3390/rs13040570).
- [38] E. Santi et al., "Soil moisture and forest biomass retrieval on a global scale by using CyGNSS data and artificial neural networks," in *Proc. IEEE Int. Geosci. Remote Sens. Symp.*, 2020, pp. 5905–5908, doi: [10.1109/IGARSS39084.2020.9323896](https://doi.org/10.1109/IGARSS39084.2020.9323896).
- [39] S. H. Yueh, R. Shah, M. J. Chaubell, A. Hayashi, X. Xu, and A. Colliander, "A semiempirical modeling of soil moisture, vegetation, and surface roughness impact on CYGNSS reflectometry data," *IEEE Trans. Geosci. Remote Sens.*, vol. 60, 2022, Art. no. 5800117.

- [40] D. Stilla, M. Zribi, N. Pierdicca, N. Baghdadi, and M. Huc, "Desert roughness retrieval using CYGNSS GNSS-R data," *Remote Sens.*, vol. 12, pp. 743, 2020, doi: [10.3390/rs12040743](https://doi.org/10.3390/rs12040743).
- [41] H. Carreno-Luengo et al., "The CYGNSS mission: On-going science team investigations," *Remote Sens.*, vol. 13, 2021, Art. no. 1814, doi: [10.3390/rs13091814](https://doi.org/10.3390/rs13091814).
- [42] N. Pierdicca, L. Guerriero, R. Giusto, M. Brogioni, and A. Egido, "SAVERS: A simulator of GNSS reflections from bare and vegetated soils," *IEEE Trans. Geosci. Remote Sens.*, vol. 52, no. 10, pp. 6542–6554, Oct. 2014.
- [43] A. Camps, "Spatial resolution in GNSS-R under coherent scattering," *IEEE Geosci. Remote Sens. Lett.*, vol. 17, no. 1, pp. 32–36, Jan. 2020, doi: [10.1109/LGRS.2019.2916164](https://doi.org/10.1109/LGRS.2019.2916164).
- [44] G. Ponnuram, T. Jagdhuber, I. Hajnsek, and Y. S. Rao, "Soil moisture estimation using hybrid polarimetric SAR data of RISAT-1," *IEEE Trans. Geosci. Remote Sens.*, vol. 54, no. 4, pp. 2033–2049, Apr. 2016.
- [45] O. Eroglu, O. M. Kurum, and J. Ball, "Response of GNSS-R on dynamic vegetated terrain conditions," *IEEE J. Sel. Topics Appl. Earth Observ. Remote Sens.*, vol. 12, no. 5, pp. 1599–1611, May 2019.
- [46] N. Rodriguez-Alvarez, E. Podest, K. Jensen, and K. C. McDonald, "Classifying inundation in a tropical wetlands complex with GNSS-R," *Remote Sens.*, vol. 11, 2019, Art. no. 1053, doi: [10.3390/rs11091053](https://doi.org/10.3390/rs11091053).
- [47] J. Bu, K. Yu, Y. Zhu, N. Qian, and J. Chang, "Developing and testing models for sea surface wind speed estimation with GNSS-R delay doppler maps and delay waveforms," *Remote Sens.*, vol. 12, 2020, Art. no. 3760, doi: [10.3390/rs12223760](https://doi.org/10.3390/rs12223760).
- [48] J. F. Munoz-Martin, N. Rodriguez-Alvarez, X. Bosch-Lluis, and K. Oudrhiri, "Stokes parameters retrieval and calibration of hybrid compact polarimetric GNSS-R signals," *IEEE Trans. Geosci. Remote Sens.*, vol. 60, 2022, Art. no. 5113911.
- [49] A. Boone et al., "Updates on the international land surface interactions with the atmosphere over the Iberian semi-arid environment (LIAISE) field campaign," *Gewex News*, vol. 31, pp. 16–21, 2021.
- [50] M. Zribi et al., "Soil surface moisture estimation over a semi-arid region using ENVISAT ASAR radar data for soil evaporation evaluation," *Hydrol. Earth System Sci.*, vol. 15, pp. 345–358, 2011.
- [51] S. Bousbih et al., "Soil texture estimation using radar and optical data from Sentinel-1 and Sentinel-2," *Remote Sens.*, vol. 11, 2019, Art. no. 1520.
- [52] M. Zribi, N. Baghdadi, N. Holah, O. Fafin, and C. Guérin, "Evaluation of a rough soil surface description with ASAR-ENVISAT radar data," *Remote Sens. Environ.*, vol. 95, pp. 67–76, 2005.



Mehrez Zribi (Senior Member, IEEE) received the B.E. degree in signal processing from the Ecole Nationale Supérieure d'Ingénieurs en Constructions Aéronautiques, Toulouse, France, in 1995, and the Ph.D. degree in remote sensing and signal processing from the Université Paul Sabatier, Toulouse, in 1998.

He is a Research Director with Centre National de Recherche Scientifique. In 1995, he joined the Centre d'Etude des Environnements Terrestre et Planétaires Laboratory/Institut Pierre Simon Laplace, Vélizy, France. Since October 2008, he has been with the

Centre d'Etudes Spatiales de la Biosphère (CESBIO), Toulouse. His research interests include microwave remote sensing applied to hydrology, microwave modeling for land surface parameters estimations and finally airborne microwave instrumentation. He has published more than 150 articles in refereed journals. He is currently director of CESBIO.



Vincent Dehaye received the M.Sc. degree in aerodynamics, energetics, and heat transfer from École Nationale Supérieure de Mécanique et d'Aérotechnique, Chasseneuil-du-Poitou, France, in 2019.

Since 2021, he has been working on data processing for the GLORI Campaign in Catalonia. He is a Research Engineer at Centre d'Etude Spatiale de la Biosphère, Toulouse, France.



Karin Dassas was born in Paris, France, in 1974. She received the Graduate degree in computer science applied to earth sciences from the "Ecole Nationale Supérieure de Géologie," Vandœuvre-lès-Nancy, France, in 1997, which corresponds to 5-year university degree (Master's degree) in earth sciences combined with engineering sciences and the master's degree in computer science from Sorbonne University (former called Université Pierre et Marie Curie), Paris, France, in 2000.

After having worked for a few years as a geophysicist for para-petroleum companies, she joined the IAS (Institut Astrophysique Spatiale, Orsay, France) in 2004 as CNRS (Centre National de la Recherche Scientifique) research engineer where she mainly did satellite data processing (L1 L2 L3 level), control-command and also on-board software for astrophysical space missions such as Planck, Herschel, Bepicolombo, JUICE. For her last mission at IAS, she was in charge of the MAJIS OBSW (Moon And Jupiter Imaging Spectrometer On Board Software) till 2021, when she joined the observation systems team at Centre d'Etude Spatiale de la Biosphère, Toulouse, France. She is currently working on GNSS-R data processing for airborne and satellite measurements.



Pascal Fanise was born in Paris, France, in 1979. He received the M.Sc. degree in electronic engineering from the University of Paris XII, Créteil, France, in 2003.

Since 2010, he has been with the Centre d'Etudes Spatiales de la Biosphère. He is currently a Instrumentation Engineer and a Technical Manager for several ground-based and airborne instruments. He is focused on microwave radiometer systems and is currently responsible of the design for the hardware architecture and experiment for GLORI reflectometer.



Michel Le Page received the technical degree in computing, the M.Sc. degree in urban geography from Paul Valéry University, Montpellier, France, in 2000, and the Ph.D. degree in remote sensing from Paul Sabatier University, Toulouse, France, in 2020.

He is an Engineer with the Institut de Recherche pour le Développement. He has more than 30 years of experience in Remote Sensing and GIS. He joined the Centre d'Etudes Spatiales de la Biosphère, Toulouse, in 2006. His research interest include the use of optical, thermal, and microwave earth observation time series for water management, including irrigation management, drought monitoring, integrated watershed modeling, and the development of end-user applications. He has published more than 50 articles in refereed journals.



Pierre Laluet received the master's degree in water sciences from the University of Rennes 1, Rennes, France, in 2019. He is currently working toward the Ph.D. degree in a remote sensing-based accounting system of agricultural water: From irrigation to drainage with the Centre d'Etudes Spatiales de la Biosphère, Toulouse, France.

He is working on the estimation of agricultural flows by combining remote sensing and hydrological models.



Aaron Boone received the B.S. degree in meteorology from Northern Illinois University, Dekalb, IL, USA, in 1988, the M.S. degree in meteorology from the Florida State University, Tallahassee, FL, USA, in 1992, and the Ph.D. degree specializing in hydrometeorology from the Université Paul Sabatier, Toulouse, France, in 2000.

He is a Research Director with Centre National de Recherche Scientifique. He worked in the Mesoscale Atmospheric Processes Branch of NASA-GSFC, USA, from 1992 to 1997. He has been with the Centre National de Recherches Météorologiques, Météo-France, since 1997, except for a stay at the Centre d'Etudes Spatiales de la Biosphère, Toulouse, from 2002 to 2003. His main research interests include land-atmosphere-hydrology interactions and land surface modeling. He has published more than 110 articles in refereed journals.